Nanoscale Advances

ROYAL SOCIETY OF CHEMISTRY

PAPER

View Article Online
View Journal | View Issue

Cite this: *Nanoscale Adv.*, 2026, **8**, 513

Machine learning-assisted characterization of cervid skin tissues with chronic wasting disease by nano-enabled Raman spectroscopic biosensing

Tianjian Tong, †*[a] Jingyi Yang, †[a] Binbin Zhu,[a] Alexis J. Frese,[bcd] M. Heather. West Greenlee,[b] Justin J. Greenlee[c] and Chenxu Yu *[a]

Chronic wasting disease (CWD) is a contagious neurodegenerative disease in cervids and its spread threatens the health of wild and farm-raised animals. A rapid screening method for CWD is in great demand. Compared to current diagnostic methods, ELISA and immunohistochemistry, Raman spectroscopic biosensing offers a potential approach to screen for CWD in real time and onsite, which is currently lacking. In this study, to evaluate the effectiveness of Raman spectroscopic biosensing for CWD detection, Raman spectra were collected by a Raman microscope as well as a portable Raman spectrometer from cervid skin tissue samples sprayed by gold nanoparticle signal enhancers collected from both heathy (*i.e.*, control, CWD-negative) and diseased (*i.e.*, CWD-positive) white-tailed deer. The spectral data were subject to analysis by two machine learning (ML) algorithms, *i.e.*, support vector machine (SVM) and artificial neural network (ANN). The results suggest that ML-assisted Raman spectroscopic biosensing can indeed offer a rapid first screening for CWD, with a highest accuracy of 88% which is comparable to existing methods. It has the potential to become a useful tool for in-field screening and detection of CWD.

Received 17th March 2025
Accepted 19th October 2025

DOI: 10.1039/d5na00252d

rsc.li/nanoscale-advances

1. Introduction

In 1967, the first case of chronic wasting disease (CWD) was identified in Colorado, USA. Since then, CWD has emerged in wild and captive cervids in North America, Norway, and South Korea.[1,2] It is a transmissible spongiform encephalopathy (TSE), or prion disease, causing fatal neurodegeneration. The disease is caused by an abnormal form of prion protein (PrP scrapie, PrP^{Sc}) that is transmitted to the host animal by exposure to excreta containing PrP^{Sc}. The PrP^{Sc} then templates the misfolding of the animal's normal cellular prion protein (PrP) to the pathologic PrP^{Sc} form that then accumulates in neural and lymphoid tissues. The conformational change of normal PrP (PrP^{c}) to PrP^{Sc} primarily involves a shift from α-helices to β-sheets within the protein structures.[3] CWD is incurable and poses a fatal threat to animal health.[4,5]

The prion gene (PRNP) encodes PrP in mammalian species. Studies of the PRNP gene in mule deer and white-tailed deer have identified several amino acid and nucleotide sequence polymorphisms. Previous studies identified PRNP polymorphisms in white-tailed deer (WTD) at codon positions 96, 132, 138, and 226.[6,7] Polymorphisms in PRNP could affect CWD susceptibility and tissue distribution in cervids,[8] impacting the degree to which cervid populations are vulnerable to disease transmission and progression.[7,8]

Chronic wasting disease has a long incubation period, which typically lasts 18 months to 3 years.[2] CWD is extremely contagious and can be transmitted from one animal to the next by contact with various excreta. CWD-infected animals have a relatively long preclinical period of disease where they show no clinical signs, but are shedding infectious material. Control of CWD within captive populations could play an essential role to protect the wild population. Thus, control of CWD depends on identification and removal of infected animals as early as possible during their preclinical period. PrP^{Sc} can be detected by immunohistochemistry (IHC), western blotting, enzyme-linked immunosorbent assay (ELISA), prion misfolding cyclic amplification (PMCA), and real-time quaking induced conversion (RT-QuIC).[4] According to USDA, IHC testing of the obex area of the brain stem or the medical retropharyngeal lymph nodes is applied for definitive diagnosis.[4,9] In mule deer, PrP^{Sc} can be detected in lymphoid tissues by IHC as early as 6 months.[9] However, the diagnostic sensitivity of the IHC test on lymphoid tissues (postmortem) reached 100% in the last 2 stages of preclinical disease but was only 36% for the earliest stage.[9]

[a]*Department of Agricultural and Biosystems Engineering, Iowa State University, Ames, IA 50011, USA. E-mail: tianjian@iastate.edu; chenxuyu@iastate.edu*
[b]*Department of Biomedical Sciences, College of Veterinary Medicine, Iowa State, Ames, IA 50011, USA*
[c]*National Animal Disease Center, USDA-ARS, Ames, IA 50010, USA*
[d]*Oak Ridge Institute for Science and Education, Oak Ridge, TN 37830, USA*
† These two authors contributed equally to this article.

Despite availability of postmortem testing, antemortem diagnostic assays are limited. The rectal mucosa biopsy sampling test (with rectoanal mucosa-associated lymphoid tissue (RAMALT)) was used to detect the CWD in white-tailed deer, in which immunohistochemical (IHC) detection of disease-associated prion protein in postmortem RAMALT biopsy samples was compared to the CWD status of each deer as determined by immunodiagnostic evaluation of the brainstem at the obex, the medial retropharyngeal lymph node, and the palatine tonsil.[10] The diagnostic sensitivity ranged from 63% to 100%, which was dependent on genotype at PRNP codon 96, and the stage of disease as assessed by obex grade. Yet, the USDA has not approved the rectal biopsy test for routine regulatory testing. Besides, this test was still an invasive test which requires cutting the skin, and needs to be completed by a trained practitioner with the animal restrained or anesthetized. It further added to the difficulty of it being applied to living animals. More recent development was to detect CWD prions in environmental and biological specimens (*e.g.*, blood,[11] saliva,[12] feces[13] *etc.*) by concentrating CWD prions with direct spiking of the sample into the protein misfolded cyclic amplification (PMCA) reactions. Reports showed that CWD prion detection in feces using PMCA was the best in the absence of sample pre-treatments, achieving diagnostic sensitivity and specificity of 54.81% and 98.46%, respectively.[13] Yet, these methods were only tested in controlled laboratory environments, not for in-field applications.[11–13]

Another technology that has been explored for CWD diagnosis and screening is real-time quaking-induced conversion (RT-QuIC), which was originally developed a decade ago for detecting abnormal form of prion proteins in diagnosis of sporadic Creutzfeldt–Jakob disease (sCJD).[14] A few studies have investigated the utility of RT-QuIC in comparison to current immunodetection assays on free-ranging cervids.[15–18] As an amplification-based molecular assay, RT-QuIC takes advantage of the propensity of the abnormal PrP^{sc} isoform to convert recombinant PrP^{C} *in vitro*,[19] which is then detected *via* fluorescence. The RT-QuIC has been reported to amply PrP^{res} seeds present in brain dilutions in the femtogram range.[17,18] Holz *et al.*[20] demonstrated that RT-QuIC is comparable to ELISA and IHC as molecular assay for CWD surveillance and screening. The RT-QuIC test has the potential to be applicable to test body fluid, blood and/or feces collected from live animals. A more recent development was a RT-QuIC assay conducted on ear pinna punches from asymptomatic mule and white-tailed deer.[21] The RT-QuIC analyses of ear samples provided apparent diagnostic sensitivity (81%) and specificity (91%) that were as good as those observed in previous analyses of rectal biopsies using RT-QuIC.[21] Christenson *et al.* also developed a nanoparticle-enhanced RT-QuIC test that could produce a result for CWD-positive tissue seeds in 4.1 hours, and no false-negatives,[22] which was much faster than all reported alternatives. However, despite the growing interest in RT-QuIC-based diagnostics, there is currently no consensus regarding the interpretation of the assay's output.[23] Similar to other molecular assays, the RT-QuIC test is sophisticated and requires skilled and trained personnel as well as specialized equipment, which further limits its accessibility to meet field testing needs.

Raman Spectroscopy is a non-destructive vibrational spectroscopic technique which provides detailed information about chemical structure, phase and polymorphism, crystallinity and molecular interactions.[20] It has been used for determining the biochemical changes in the bio-macromolecules of cells and tissues, as well as body fluids, like blood plasma/serum and urine, for the diagnosis of various diseases, with the help of machine-learning (ML) based data analysis.[24–31] Among them, diseases caused by amyloid accumulation,[26] and neurodegenerative Parkinson's disease[31] are especially relevant as they are, like CWD, protein misfolding diseases. As CWD primarily affects the brain, it remains to be seen whether PrP^{Sc} related changes could be detected in skin tissues, which could then serve as a basis for the development of non-invasive CWD screening methods.

In this study, to evaluate the effectiveness of ML-assisted Raman spectroscopic biosensing as a tool for CWD diagnosis on skin tissues, Raman spectra from skin tissue samples from both heathy (*i.e.*, control, CWD-negative) and diseased (*i.e.*, CWD-positive) cervids (whitetail deer) were collected using both a dispersive Raman microscope and a portable Raman spectrometer. To enhance the Raman signal, gold nanoparticle serving as surface-enhanced Raman spectroscopic (SERS) enhancers were sprayed onto tissue surfaces before signal acquisition. The spectral data were then classified by two ML algorithms, support vector machine (SVM) and artificial neural network (ANN). The results suggest that SERS biosensing in conjunction with ML can indeed offer a rapid first screening for CWD, with the highest accuracy of 88%, comparable, or even superior, to existing methods reported in literature.

2. Materials and methods

2.1 Skin tissue samples

Two sets of samples (A and B, described below) were used for this study. CWD is considered a highly contagious disease, and CWD samples are strictly regulated by the USDA. Therefore, the design of our approach must be flexible to accommodate the limited availability of samples.

The first set of samples (set A) were paraffin-embedded skin samples collected from white-tailed deer (*Odocoileus virginianus*, WTD) in captivity. Ear notches (~1.0 cm × 1.0 cm pieces from the middle of the ear) were taken post-mortem from farmed WTD that were under quarantine with a history of CWD. The study population consisted of 11 positive and 13 non-detect deer (referred to as "negative" from here on); all were males. Each sample was put into 10% neutral buffered formalin and held in formalin for 6 months until they were embedded in paraffin. All work was done in accordance with and had the approval of the Iowa State University Institutional Biosafety Committee (IBC-19-021). After embedding, 3–4 μm sections for spectral acquisition with a dispersive Raman microscope (DXR Raman microscope, Thermo Scientific Inc., Madison, WI, USA) were mounted on gold slides.

The section thickness of 3–4 μm was chosen for two reasons: firstly, this thickness would allow the sections to be de-paraffined easily, as the thickness of the section went up, more paraffin (hence stronger paraffin signals) remained with the sample after de-paraffining (data not shown); and secondly, as the sections were mounted onto gold-coated slides, the 3–4 μm thickness was sufficient to yield good quality spectra. The Raman spectra were acquired with the DXR microspectrometer using a 100x objective with a 1.25 NA, at a spectral resolution of 1 cm^{-1}, with a 780 nm excitation laser.

The second set of samples (set B) were skin samples collected during a depopulation of a farmed cervid premises that went through the diagnostic screening by U.S. Department of Agriculture Animal and Plant Health Inspection Service (APHIS) Veterinary Services. They were also ear notches taken post-mortem, with similar size to the samples in set A. The study population consisted of 10 positive and 10 negative deer, the population was sex-blind, as no sex information was available. Each sample was put into 10% neutral buffered formalin and held in formalin until spectral acquisition. They were rinsed with distilled water for 15 min before spectral acquisition. To enhance the Raman spectra collected from the tissue samples, Au nanoparticle solution (20 nm spherical particles at 1 nM PBS buffer, cat. 753 610, Sigma-Aldrich, St. Louis, MO, USA) were sprayed onto the surfaces of the tissue samples, and then the samples were air-dried. These samples were not paraffin-embedded. Spectral acquisition using a portable Raman spectrometer (iRaman plus, Metrohm USA Inc., Riverview, FL, USA) was done on the cut face of the formalin-fixed tissue samples.

All animals investigated in this study, including both the first set and the second set, were screened by ELISA and confirmed by immunohistochemistry using samples of brain stem at the level of the obex, retropharyngeal lymph node, and palatine tonsil, for their positive/negative status following the diagnostic procedures adopted by USDA regulation. The animals were then labelled as either positive or negative, and the ear notch skin of each animal was then collected as described later for Raman spectroscopic analysis. The standard screening using immunohistochemistry was 100% accurate for animals that died from CWD. Both ELISA and immunohistochemistry were conducted with brainstem, lymph node and/or palatine tonsil, which were acquired from carcasses of animals, they did not work with skin tissues.

2.2. Data acquisition with Raman micro-spectroscopy and portable i-Raman spectrometer

Raman spectra were collected from each of the Au-slide mounted tissue section samples before/after de-paraffinization. Paraffin wax used for tissue embedment was also measured with in the same spectral range using both spectrometers to identify key paraffin peaks. Samples were deparaffinized to reduce the back-ground interference from the paraffin. The procedure was as follows: 10 min incubation in xylene, 10 min incubation in 100% ethanol, 10 min incubation in 95% ethanol, 10 min incubation in 70% ethanol and then 10 min incubation in DI water.

After deparaffinization, these de-paraffined skin samples (DSS) were subject to data acquisition using 780 nm laser with 14 mW laser power. Aperture is 25 μm pinholes. 20 spectra were acquired from each sample. Each spectrum was obtained with 20 seconds exposure time and 2 replicates.

The ultimate goal is to develop a rapid-screening method for CWD that can be applied for quick, onsite interrogation. Hence, a portable Raman spectrometer was also used to directly collect spectral data from WTD tissue samples. The portable Raman spectrometer used a laser excitation of 785 nm with 340 mW nominal power at the exit of the fiber optical probe. The laser power was adjusted to 10% of the full power to minimize potential photo damage to the samples. The fiber probe (1.0 m long, with 105 μm core for excitation, and 300 μm core for collection) collects photonic signals through a shaft with 9.42 mm diameter from a large 4 mm diameter measurement area. Spectra were collected 65 and 2800 cm^{-1}, with a spectral resolution at 3.5 cm^{-1}. 10 spectra were acquired from each tissue sample. Each spectrum was obtained with 5 second integration time and 2 replicates. The small number of spectra (10) per sample were selected purposedly to mimic situations in practical applications for in-field screening, where not much time would be available to acquire large numbers of spectra. The short integration time (5 s) was used to minimize photo-damage to the samples, this would be important for eventually developing an *in vivo* screening method for live animals.

All spectra collected with both XDR and iRaman systems were automatically corrected for dark current and background noises (*e.g.*, optical system) with the system software provided by the manufacturers. Data acquisition was conducted in a dark room to minimize ambient light. The spectra were then subjected to data preprocessing described below.

2.3 Data preprocessing and PCA

The data preprocessing was then conducted, including smoothing, polynomial baseline correction, and normalization. Smoothing was performed with a 10-point moving average; baseline correction was implemented based on an iterative polynomial fitting;[32] and normalization was conducted using the function in the open source "scikit-learn" machine learning library in Python.

After preprocessing, principal component analysis (PCA) was conducted to reduce the dimensionality of data, increase interpretation, and minimize information loss. PCA has been used in ML-assisted spectroscopic classification for differentiation of a variety of disease-related tissues, such as normal *vs.* malignant mucosal tissues,[24] parathyroid tissue,[25] breast tumor tissues,[28] glaucomatous retina,[29,30] and brain tissues with Alzheimer disease.[31,33] After PCA transformation of the spectral data, classification models were constructed based on ML algorithms to differentiate disease positive *vs.* negative samples, and PCA transformed data were randomly assigned into training and testing groups to evaluate the classification accuracy.

2.4 ML-assisted classification

Classification is a supervised ML process of predicting the class of given data points, namely, negative or positive for CWD.

There are a lot of ML classification algorithms available, including linear and logistic regression, multi-class classification, decision trees, SVM, and ANN *etc.* In this study, SVM and ANN were chosen as the ML algorithms for developing the classification models, and their performance was compared for the same group of samples. As shown in Fig. 1, the original spectral data went through pre-processing, and the de-noised data were then subject to PCA-based dimension reduction. The PCA data were then fed to either the SVM or the ANN models. These two models were trained independently, and the classification performance of the two models was then compared.

2.4.1 SVM. A SVM is a supervised machine learning method used for classification, regression, and outlier detection, which was first developed by Vapnik and his group at AT&T Bell Laboratories.[34] The objective of the SVM method is to find a hyperplane in an *N*-dimensional space that distinctly classifies the data points into two clusters. A good classifier is achieved by the hyperplane that has the largest distance to the nearest training data points of any class (so-called functional margin), since in general the larger the margin the lower the generalization error of the classifier. In this study, classifiers are constructed by sklearn.svm.SVC in Python. Giving training vectors $x_i \in \mathbb{R}^p, \quad i = 1, \ldots, n$, in two classes, and a vector $y \in \{1,-1\}^n$, the goal is to find $\omega \in \mathbb{R}^p$ and $b \in \mathbb{R}^p$ such that the prediction given by sign $(\omega^T \phi(x) + b)$ is correct for most samples. SVC solves the following primal problem:[36]

$$\min_{\omega,b,\zeta} \frac{1}{2}\omega^T\omega + C\sum_{i=1}^{n}\zeta_i$$
$$\text{subject to } y_i\left(\omega^T\phi(x_i) + b\right) \geq 1 - \zeta_i, \zeta_i \geq 0, \quad i = 1, \ldots, n \tag{1}$$

2.4.2 ANN. An ANN is a series of algorithms appropriate for complex classification and pattern recognition problems in a set of data through a process that mimics the operation of the human brain. The feedforward ANN was utilized for the data classification in this research, shown in Fig. 2. This class of network is composed of one input layer that receives the vector to be classified, one output layer that presents the classification results and a set of intermediate layers named hidden layers. In this model, the number of hidden layers is 8, and the number of neurons in each intermediate layer decreases to half of the previous layer.

The SVM and ANN classifiers were developed using Python. The code could be downloaded at https://github.com/juliachu216/Research.

3. Results and discussions

3.1 Analysis of Raman spectra collected from the skin samples

Spectra of negative and positive skin samples prior to deparaffin exhibited five obvious peaks at 1067 cm^{-1}, 1136 cm^{-1}, 1300 cm^{-1}, 1445 cm^{-1}, and 1464 cm^{-1}. However, spectrum of paraffin wax contains ν(CC) band around 1107 cm^{-1} and ν(CO) features around 1060 cm^{-1}, CH_2 deformation contributes peaks at 1445 cm^{-1}, and 1464 cm^{-1}.[37] Thus, the strong background signal of the paraffin wax could interfere with the spectral signals from the cellular components including PrPSc prions. As shown in Fig. 2a, average spectrum from positive paraffin embedded skin samples cannot be differentiated from that of negative skin samples by simple visual inspection. To highlight major differences between the two sample groups, the welch's *t*-test using *p*-value less than 0.01 as a significance level was utilized to identify peaks that showed significant differences. Only the peaks at the 1420–1450 cm^{-1} range had significant *p*-values of ~0.005, which as mentioned could be due to the paraffin wax and did not reflect any physiological differences between the two groups.

Since paraffin wax seemed to dominate the Raman spectra collected from the tissue section samples, a de-paraffinization procedure was used to remove the paraffin. Fig. 2b showed average spectra of negative and positive deparaffinized skin samples, which were significantly different from the spectra of paraffin skin samples. The welch's *t*-test was again utilized to analyze the peaks showing significant differences between the P/N groups. Five peaks were identified at 863 cm^{-1}, 944 cm^{-1},

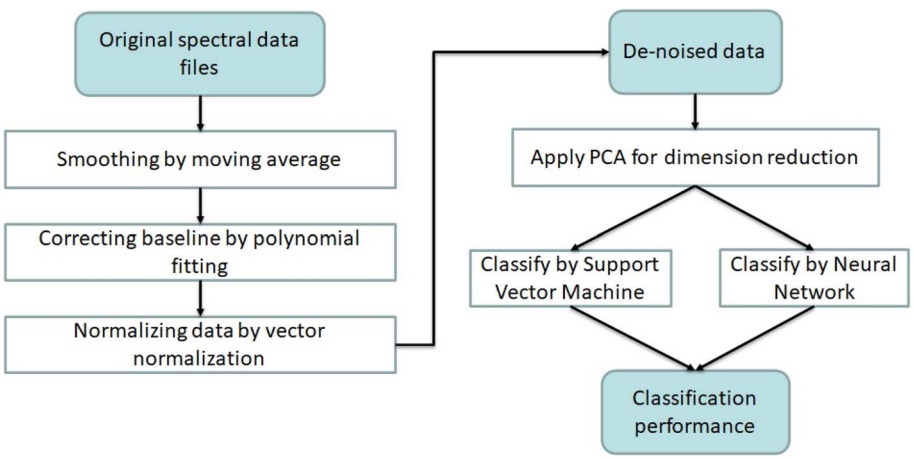

Fig. 1 A flowchart of the data analysis process used in the ML-assisted CWD screening.

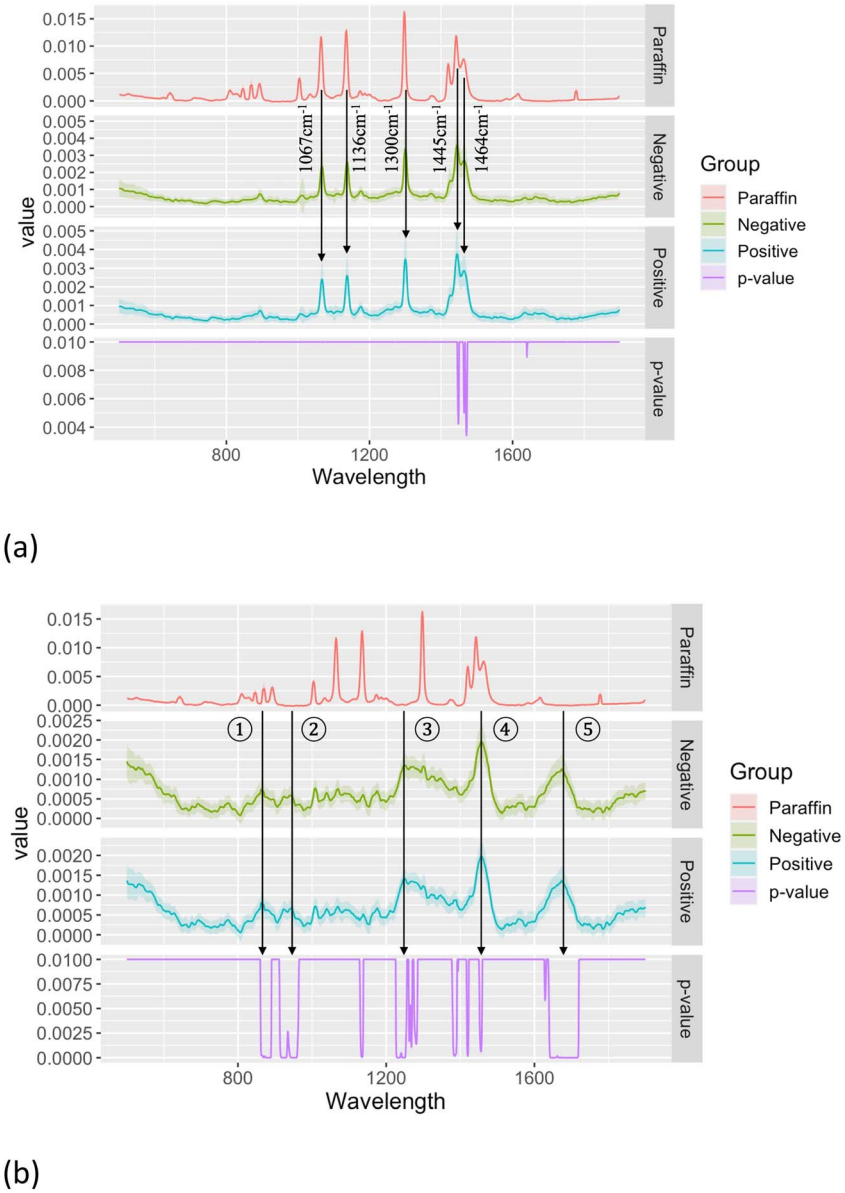

Fig. 2 Average spectra of negative (260 spectra in total) and positive (220 spectra in total) PSS of set A with *p*-value of *t*-test. (a) Before de-paraffin; (b) after de-paraffin. Shaded areas around the average spectra showed the standard deviation of all the spectra in the group. Peaks labeled in (b) are listed in Table 1.

1252 cm^{-1}, 1457 cm^{-1}, and 1673 cm^{-1}, none of these peaks belonged to paraffin. The amide I band was identified by the characteristic peak around 1673 cm^{-1}, which was associated with secondary structure such as β turns,[35,37] and a strong band at 1252 cm^{-1} in the amide III region was also reported to be related to secondary (*e.g.*, β-sheet) structure of proteins.[35,37] The band of CH_2 and CH_3 bending in proteins was observed around 1457 cm^{-1}. The peak at 944 cm^{-1} was assigned to the C–C skeletal mode of α-helix structure. The bands associated with tyrosine were observed around 863 cm^{-1}.[26,35,37] Changes of these peaks on positive samples, as listed in Table 1, appeared to be correlated to the structural changes of PrP^{Sc} prions (*e.g.*, α-helices to β-sheets) in the skin samples.[38]

When the portable Raman spectrometer was used to test direct spectral acquisition, since the samples were NOT embedded in paraffin, a de-paraffinization process was not needed. In addition, gold nanoparticles were sprayed onto the exposed tissue surface, and then air-dried to generate a thin-layer of Au nanoparticles on the surface to serve as enhancers to the Raman signals, as surface enhanced Raman spectroscopy (SERS) could lead to 10^6–10^7 times of enhancement to spectral signals collected from nanoparticle-bound cellular samples.[39,40] However, with simply spraying the Au particles onto the samples, the spectra collected were at best a mixture of SERS features around hotspots, and spontaneous Raman features. Our reasoning was that even with a limited level of enhancement, it would still help with the differentiation between CWD

Table 1 The wavelength, intensity, *P*-value and assignment of peaks for key Raman bands in Positive/Negative DSS samples

	Raman shift (cm^{-1})	Peak intensity (negative)	Peak intensity (positive)	*P*-value	Assignments
1	863	0.000743	0.000809	0.000283	Tyrosine
2	944	0.000595	0.000672	0.000655	C–C α-helix in proteins
3	1252	0.00135	0.00141	0.000782	Amide III
4	1457	0.00196	0.00199	0.000874	CH_2, CH_3 bending in proteins
5	1673	0.00125	0.00136	0.000581	Amide I

positive/negative samples. As shown in Fig. 3, the average spectra for both negative and positive tissues from set B bear great similarities to the spectra of the de-paraffined samples of set A (shown in Fig. 2b), indicating the effectiveness of the de-paraffin processed used for the first set of samples. A closer investigation revealed that among the 5 bands showing significant differences between the negative and positive groups for set A, four bands (no. 1, 3, 4 and 5) also showed significant differences between the negative and positive samples of set B. Only band no. 2 at ~944 cm^{-1} did not show a significant difference among the two groups, with a *P*-value of >0.01. In addition, three more peaks exhibited significant differences: peak no. 6 at ~1060–1085 cm^{-1}, peak no. 7 at ~1310 cm^{-1}, and peak no. 8 at ~1500–1550 cm^{-1}. All three peaks showed significant differences with *P*-values of <0.005. Among these three, peak no. 6 is assigned to C–C skeletal stretching of lipids, peak no. 7 at ~1310 cm^{-1} is assigned to C–O stretching of aromatic ester, and peak no. 8 at 1500–1550 cm^{-1} is assigned to strong N–O stretching. These 7 peaks showing significant differences could provide the basis for successfully differentiating samples between the CWD positive and negative groups.

3.2 Classification of the spectral data of samples using SVM and ANN

Principal component analysis (PCA) was applied for dimensionality reduction and features extraction for these two sets of data (post de-paraffinization). It is essential to estimate how many principal components (PCs) are needed to describe the spectral data. This can be determined by looking at the cumulative explained variance ratio as a function of the number of components. PCA on the deparaffinized datasets (DSS) showed that ten PCs were responsible for less than 50% of the total variance, 50 PCs only retained about 70% of the variance, and 200 PCs accounted for almost 100% of the variance. Discrimination between negative and positive groups still cannot be achieved easily with a simple 2-D projection plot. As shown in Fig. 4a and b, with 1st PC (PC0) and 2nd PC (PC1), no separation of the two groups was visible for either the microscopic (deparaffinized) or the portable Raman (paraffin embedded block) data sets.

To classify the deparaffinized spectral data (DSS), 520 spectra were used among which 272 spectra were from negative samples, and 248 spectra were from positive samples. Then, 75% of all spectra from each group (204 negative, 186 positive) were randomly selected from the set, and these 390 spectra were used as the training set for the SVM classifiers. The remaining 25% of the spectra (130 with 68/N and 62/P) were used as a testing set to evaluate the accuracy of the SVM models. 10 repetitions with separate training/testing sets were conducted to calculate the average accuracy.

SVM classifiers were constructed by using 10 PCs, 50 PCs, 200 PCs, and the original deparaffinized spectra (DSS), respectively. The SVM was implemented with Python, and a grid search was performed first to find the best SVM for each of the

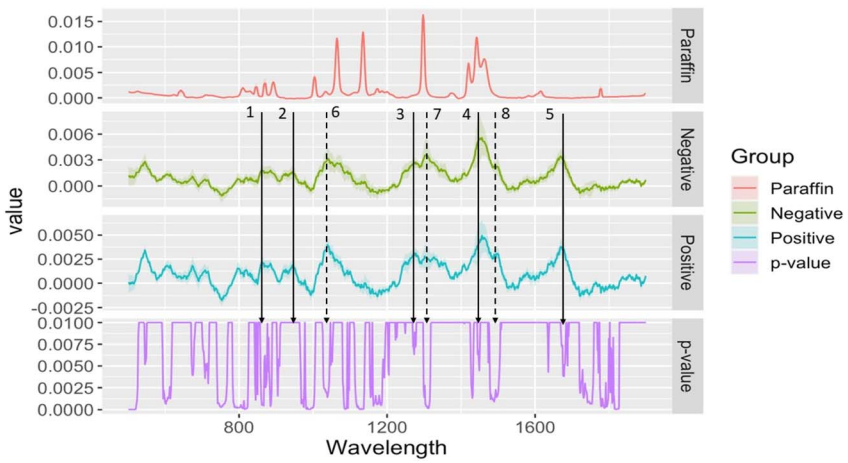

Fig. 3 Au-enhanced average spectra of negative (150 spectra in total) and positive (150 spectra in total) tissue samples acquired using a portable Raman spectrometer with *P*-value of *t*-test. Shaded areas around the average spectra showed the standard deviation of all the spectra in the group. Peaks labeled are listed in Table 1.

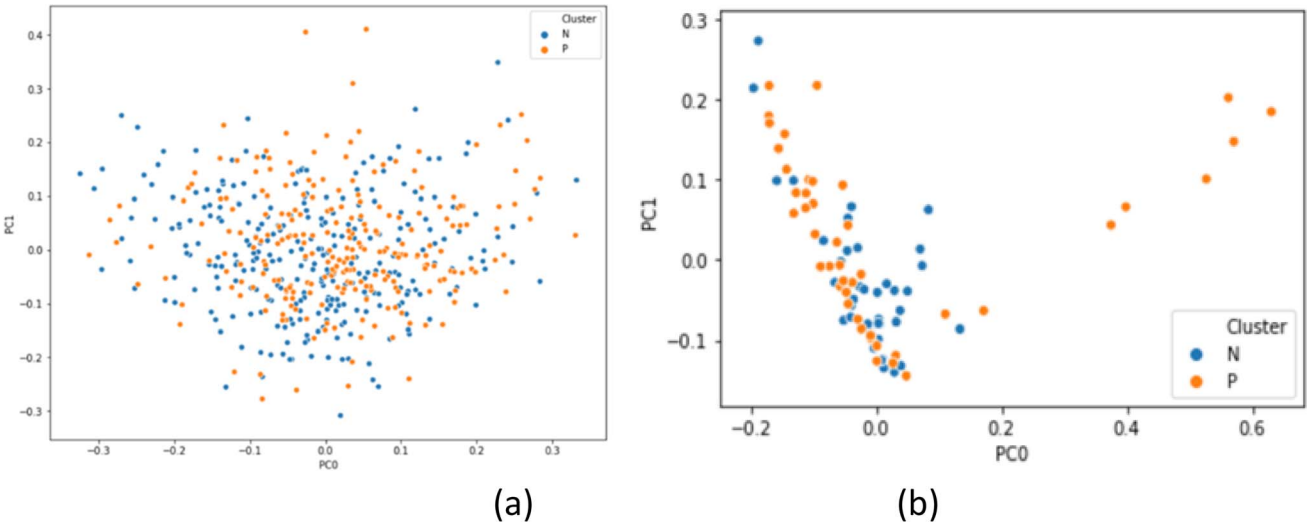

Fig. 4 Clustering of PC0 and PC1 for negative and positive (a) deparaffinized skin and (b) paraffin-embedded skin tissue.

dataset, which are listed in Table 2. For the 10 PCs dataset, a polynomial kernel (poly) was used, for the other three datasets, a radial basis function (RBF) kernel was used. 10 replicates (each with re-assigned training/testing sets) were run to calculate the average accuracy for each dataset. The classifier constructed by 50 PCs yielded the best prediction accuracy, at 0.731.

In ANN, the same 10 PCs, 50 PCs, 200 PCs, and the original deparaffinized skin spectra (DSS; 1556 variables) datasets were used, and the 75%/25% random split was again used for training/testing sets. 10 repetitions were run and the average prediction accuracies were calculated. The results were improved accuracy for all four datasets for the DSS (and for the PSS data, Table 3). The classifier with the lowest accuracy was the 200 PCs' model. The 10 PC classifier and the 50 PC classifier both yielded an accuracy of 0.762, all were better than that of SVM models.

The spectroscopic method was developed to eventually interrogate skins of live animals, so the de-paraffined samples were a better representation of what would be present on a live animal. The 76.2% classification accuracy, hence, is an indicator for potential diagnostic applications. It should be noted that micro spectroscopic investigation was more susceptible to localized chemical variations within the skin biopsy samples, as the spectral acquisition was from a small area (a spot of 10 μm × 10 μm), which could further reduce the classification accuracy. For microscopic Raman investigation, to improve the classification accuracy, either more data are collected from more localities randomly selected from the tissue surface, or mapping (*i.e.*, Raman imaging) is explored to generate chemical images of the surface, using Raman peaks identified in Table 1, then subject the Raman images to ML-assisted data analysis. The main drawback of Raman mapping was the long time (2–3 hours) it takes to create an image for even a small area of 10 mm × 10 mm. It is expected that better classification accuracy may be possible with larger spectral acquisition areas in fiber-optic based portable Raman systems, which would be more suitable for on-site deployment for in-field CWD screening.

Fig. 5 showed the receiver operating characteristic (ROC) curves for both the SVM and ANN models. To compare the ROCs for the best performance, the ROCs shown were for classifiers with 50 PCs. The areas under the curve (AUCs) were calculated for both SVM and ANN models, with either DSS or PSS samples. Fig. 5a shows the ROC for the SVM classifier for PSS samples, the AUC was 0.679; Fig. 5b shows the ROC for the SVM classifier for the DSS samples, and the AUC was 0.731; apparently the classification accuracy of the SVM model was better for the DSS samples than that of the PSS samples, consistent with the results reported earlier. Fig. 5c and d show the ROCs for the ANN model, with PSS and DSS samples, respectively. Similar trend as for the SVM model was observed. The classification was more accurate for the DSS samples (AUC = 0.807) than that of the PSS samples (AUC = 0.695), further confirmed our discussion on the effects of the de-paraffining. For the same types of the samples, the AUCs of the ANN model were also slightly larger than that of the SVM model, suggesting that overall ANN model performed slightly better than that of the SVM model. Nonetheless, the AUCs for the de-paraffined samples (DSS) were 0.731 and 0.807

Table 2 Support vector machine results for DSS and PSS

	10 PCs	50 PCs	200 PCs	Spectral data
SVM Model kernel	poly	RBF	RBF	RBF
SVM Model parameters	degree = 5, coef0 = 2	C = 10, gamma = 1	C = 100, gamma = 0.1	C = 100, gamma = 0.1
Accuracy, DSS	0.700	0.731	0.692	0.685
Accuracy, PSS	0.662	0.685	0.600	0.585

Table 3 Artificial neural network results for DSS and PSS

	10 PCs	50 PCs	200 PCs	Spectral data
Accuracy, DSS	0.762	0.762	0.723	0.746
Accuracy, PSS	0.700	0.723	0.685	0.692

for the SVM and ANN classifiers, respectively, which were both acceptable as classifiers.

In addition, taking a closer look at the ROCs for the DSS samples, when the sensitivity (*i.e.*, the positive rate) reached 0.8, the specificity for the SVM classifier was 0.6 (*i.e.*, 1-false positive rate), and for the ANN classifier was 0.74, also suggesting that the ANN model performed better than that of the SVM model. Similar trend was also observed for the data set no. 2, which was the unparaffined skin tissue samples. Overall, the ANN classifier worked better than the SVM classifier for our samples, and both yielded acceptable classification accuracy.

3.3 Classification of the tissue spectral data of samples from set no. 2 using SVM and ANN

The dataset for samples in set B had 200 spectra in total, the training set had 150 spectra (75 negative/75 positive), and the testing set had 50 spectra (25 negative/25 positive). As in the case of the set A samples, the split between training/testing sets was random, and 10 replicates were conducted with reassignment of training/testing sets for each replicate.

A PCA was conducted for dimensionality reduction and features extraction as well with the set B spectral data. 50 PCs were responsible for 91.3% of the total variance. Classifiers (SVM and ANN) were constructed using 10 PCs, 50 PCs, and the original spectral data, respectively. A grid search for SVM

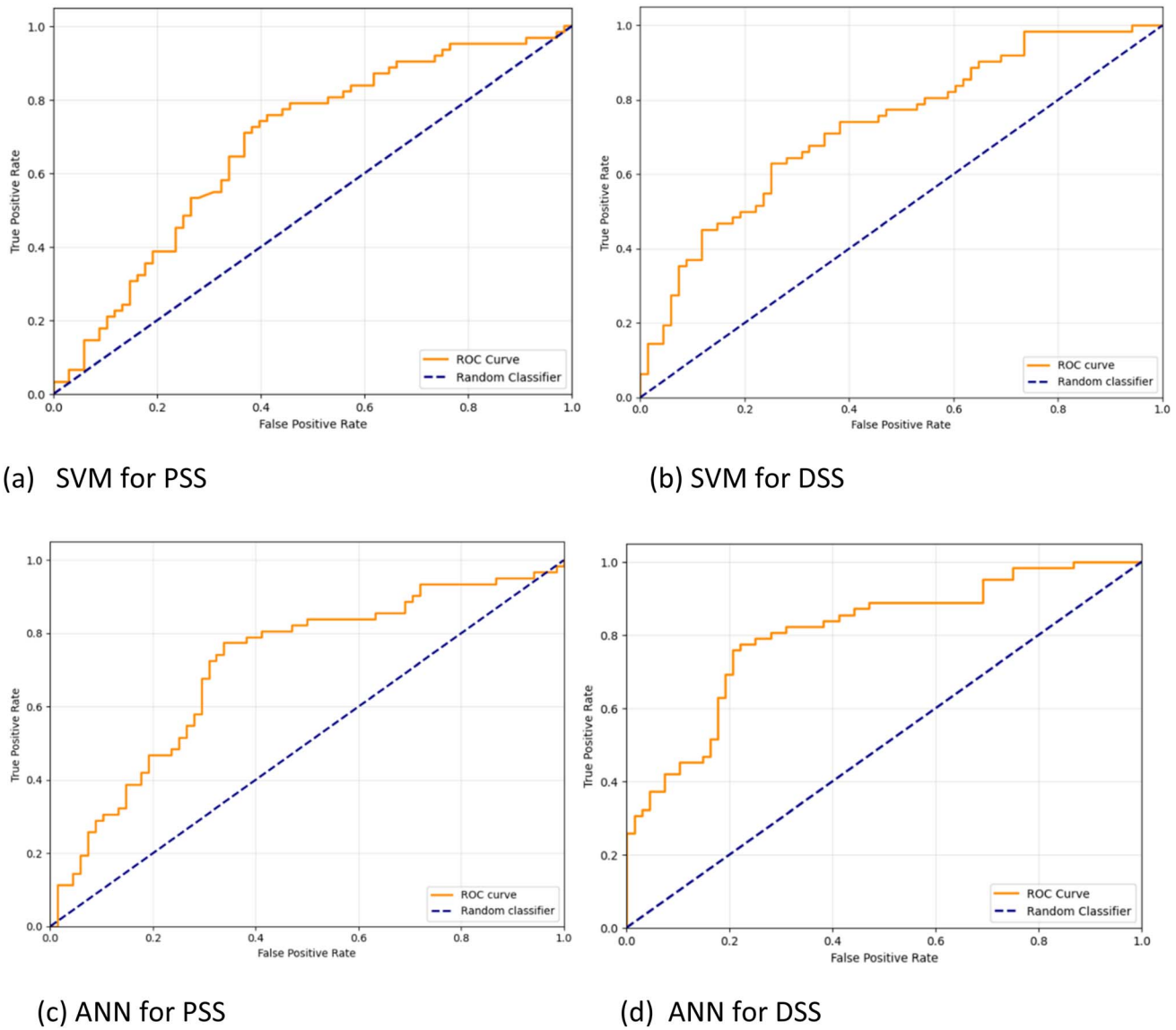

Fig. 5 ROC curves for the best performing classifiers with 50 PCs (a) SVM for PSS samples; (b) SVM for DSS samples; (c) ANN for PSS samples; (d) ANN for DSS samples.

Table 4 SVM and ANN results for FFPE samples

	10 PCs	50 PCs	Whole spectrum
SVM Model kernel	rbf	rbf	rbf
SVM Model parameters	C = 1000, gamma = 0.1	C = 1000, gamma = 0.1	C = 1000, gamma = 0.1
Accuracy, SVM	0.840	0.720	0.720
Accuracy, ANN	0.840	0.880	0.720

suggested that the radial basis function (RBF) kernel yielded the best classification accuracy for all datasets.

As shown in Table 4, SVM classifiers constructed by 10 principal components yielded the best prediction accuracy, which reached 0.84.

The prediction accuracy of the ANN algorithm also improved in all three datasets for the set B compared to the DSS data from set A. The classifier with the highest accuracy was with the 50 PCs dataset, which reached 0.88. 10 PCs' classifier yielded 0.84 accuracy, and the lowest accuracy was with whole spectral data, at 0.72. The confusion table for the best performer (accuracy 0.88, 50 PC dataset with ANN) was shown in Table 5. The classification for the CWD positive samples had an average accuracy slightly higher than that for the negative samples, suggesting the Raman method has the ability to detect CWD positive samples with the highest accuracy, which is very desirable as missing a negative CWD case is less troublesome than missing a positive one.

With the portable Raman spectrometer, laser spot diameter at the focal plane of the fiber probe was 85 μm (comparing to 1–2 μm on the Raman microscope used for DSS and PSS samples), with a measurement area on the tissue sample of 4 mm diameter. Larger laser spot translates into a bigger sampling area on the tissue sample, which will collect Raman photons from more cells and significantly reduce the variations due to local compositional differences thus, the portable Raman spectrometer system would be more suitable for onsite deployment for in-field CWD screening.

In addition, the application of surface enhancement *via* Au nanoparticles could have increased the signal intensity collected from the tissue samples and contributed to the increase of the classification accuracy. The approach developed involves easy spraying of Au nanoparticle solution onto the skin tissue sample, which can be readily applied to live animal testing. In this scenario, the skin underneath the ear (where there is not much hair) of a sedated live animal will be shaved to expose the skin, and the Au nanoparticle solution will then be sprayed onto it. Once the surface dries up, spectral acquisition can be conducted. It is expected that the whole process should take less than 30 minutes for an animal, and a field worker can be easily trained to undertake the task. As mentioned earlier, this simple approach does not assure acquisition of SERS signals, rather it is most likely that a mixed spectrum of SERS and spontaneous Raman will be obtained. However, as shown in this study, these spectral data contained enough information to allow a rapid yet relatively accurate differentiation of the CWD positives from the CWD negatives. Until now, there is no method that can offer a fast screening for CWD in live animals. ELISA, PMCA and similar molecular tests can provide accurate CWD diagnosis, but these methods interrogate samples obtained from the brain stem or the lymph nodes of the animal, which usually are collected from an animal that was already dead. Nano-QuIC[22] was reported to have the potential of analyzing samples collected from live animal, but even with its "2.5X reduced" time comparing to regular RT-QuIC, the Nano-QuIC test still took 4.1 hours to yield a result.[22] In comparison, Raman-based test can be done within 10 minutes. The only test that has been tested in field for live animals was the rectal mucosa biopsy sampling test (RMBST), which requires a biopsy sample to be taken from the rectal mucosa, a quite invasive procedure comparing to the foreseen approach with the Raman screening. Besides, the accuracy of the RMBST was dependent on the stage of the disease, it was reported at only 36% for early CWD cases.[8] The Raman approach demonstrated here compared favorably to the RMBST, although more validation is certainly needed, and *in vivo* testing is the natural next step.

What would also be helpful is to further explore the powers of deep learning. The simple ANN reported in this study offered reasonable classification accuracy. The simple ANN and SVM we used in this study were designed for homogeneous data sets (*i.e.*, Raman spectral data). With deep learning and more advanced algorithms, it would be possible to pool heterogeneous data sets together, for example, imaging data showing motion postures of the animal in question, metabolic panel for the animal in question, *etc.*, can be used alongside with Raman spectral data to train a ML-powered classification model to achieve better prediction accuracy.

The portable Raman spectrometer costs at ~$15 000 in the current market, the amount of Au nanoparticles used for each test is less than $1. The Raman screening could be quite cost effective for deer farmers who need to conduct screening for their herds, on a year-round basis. This approach, once fully developed, could add a powerful tool to the battle against CWD.

Table 5 Confusion table of average prediction accuracy for the ANN test with 50 PCs

	Actual positive	Actual negative
Predicted positive	0.91	0.09
Predicted negative	0.15	0.85

4. Conclusions

In this study, two Raman spectrometer systems, A Thermo XTR Raman micro spectrometer, and a Matrohm i-Raman plus

portable Raman spectrometer, were utilized to compare CWD-positive skin tissues to CWD-negative samples of white-tail deer. After spectral collection, support vector machine (SVM) and artificial neural network (ANN) classifiers were generated based on PCs calculated from the spectral data sets to classify the spectra kept in testing sets into positive/negative groups. Data collected with a Raman microscope from deparaffinized skin tissue samples (DSS) yielded a 76.2% classification accuracy with the ANN model, which was the highest among the results obtained for the DSS samples. In comparison, the discrimination of paraffined skin tissues (PSS) using Raman microspectroscopic data was not as good, suggesting for microscopic spectral acquisition, the presence of paraffin would interfere with the signals from the actual biological samples to complicate the differentiation and classification. In addition, the microscopic spectra data were more susceptible to intra-tissue variations due to spot-to-spot differences. A spectral acquisition technique with larger sampling area was expected to generate better classification accuracy by minimizing intra-tissue variations, which was confirmed with the portable Raman spectrometer. The portable Raman spectrometer smoothed over intra-tissue variants due to a bigger laser spot diameter at focal plane. In addition, Au nanoparticles were utilized to generate surface enhanced Raman scattering (SERS) to further improve the spectral signals. By this approach, an artificial neural network (ANN) generated the best classification accuracy at 88%. These results suggest that Raman spectroscopic screening potentially can offer a rapid, and quite accurate screening of CWD in skin biopsies for onsite identification of diseased animals.

Conflicts of interest

The authors declare no conflict of interest.

Data availability

The code for the SVM and ANN classifiers developed in this project could be downloaded at https://github.com/juliachu216/Research.

Acknowledgements

The authors would like to acknowledge Dr Tracy Nichols from the U.S. Department of Agriculture Animal and Plant Health Inspection Service (APHIS) Veterinary Services Cervid Health Team for facilitating collection and use of the samples used in this study. The authors would like to acknowledge SENSIS agency and USDA-ARS (award no. 019636-00001) for funding that partially supported the study.

References

1 Norwegian Veterinary Institute, Chronic wasting disease, Oslo (Norway), Norwegian Veterinary Institute, [cited 2020 Oct 30], available from, https://www.vetinst.no/en/surveillance-programmes/chronic-wasting-disease.
2 T. Y. Kim, H. J. Shon, Y. S. Joo, U. K. Mun, K. S. Kang and Y. S. Lee, Additional cases of chronic wasting disease in imported deer in Korea, *J. Vet. Med. Sci.*, 2005, **67**(8), 753–759.
3 Z. Zhou and G. Xiao, Conformational conversion of prion protein in prion diseases, *Acta Biochim. Biophys. Sin.*, 2013, **45**(6), 465–476, DOI: 10.1093/abbs/gmt027.
4 D. Gavier-Widén, M. J. Stack, T. Baron, A. Balachandran and M. Simmons, Diagnosis of transmissible spongiform encephalopathies in animals: a review, *J. Vet. Diagn. Invest.*, 2005, **17**(6), 509–527.
5 A. R. Castle and A. C. Gill, Physiological functions of the cellular prion protein, *Front. Mol. Biosci.*, 2017, **4**, 19.
6 K. I. O'Rourke, T. E. Besser, M. W. Miller, T. F. Cline, T. R. Spraker, A. L. Jenny, *et al.*, PrP genotypes of captive and free-ranging Rocky Mountain elk (Cervus elaphus nelsoni) with chronic wasting disease, *J. Gen. Virol.*, 1999, **80**(Pt 10), 2765–2769.
7 G. J. Raymond, A. Bossers, L. D. Raymond, K. I. O'Rourke, L. E. McHolland, P. K. Bryant 3rd, *et al.*, Evidence of a molecular barrier limiting susceptibility of humans, cattle and sheep to chronic wasting disease, *EMBO J.*, 2000, **19**(17), 4425–4430.
8 A. Otero, C. D. Velasquez, C. Johnson, A. Herbst, R. Bolea, J. J. Badiola, *et al.*, Prion protein polymorphisms associated with reduced CWD susceptibility limit peripheral PrPCWD deposition in orally infected white-tailed deer, *BMC Vet. Res.*, 2019, **15**, 50.
9 C. J. Sigurdson, E. S. Williams, M. W. Miller, T. R. Spraker, K. I. O'Rourke and E. A. Hoover, Oral transmission and early lymphoid tropism of chronic wasting disease PrPres in mule deer fawns (Odocoileus hemionus), *J. Gen. Virol.*, 1999, **80**(10), 2757–2764.
10 B. V. Thomsen, D. A. Schneider, K. I. O'Rourke, T. Gidlewski, J. McLane, R. W. Allen, *et al.*, Diagnostic accuracy of rectal mucosa biopsy testing for chronic wasting disease within white-tailed deer herds in North America: effects of age, sex, polymorphism at PRNP codon 96, and disease progression, *J. Vet. Diagn. Invest.*, 2012, **24**(5), 878–887.
11 C. Kramm, P. Soto, T. A. Nichols and R. Morales, Chronic wasting disease (CWD) prion detection in blood from pre-symptomatic white-tailed deer harboring PRNP polymorphic variants, *Sci. Rep.*, 2020, **10**, 19763.
12 K. A. Davenport, C. E. Hoover, N. D. Denkers, C. K. Mathiason and E. A. Hoover, Modified protein misfolding cyclic amplification overcomes real-time quaking-induced conversion assay inhibitors in deer saliva to detect chronic wasting disease prions, *J. Clin. Microbiol.*, 2018, **56**(9), e00947–18.
13 F. Bravo-Risi, P. Soto, R. Benavente, T. A. Nichols and R. Morales, Dynamics of CWD prion detection in feces and blood from naturally infected white-tailed deer, *Sci. Rep.*, 2023, **13**, 20170.
14 R. Atarashi, K. Sano, K. Satoh and N. Nishida, Real-time quaking-induced conversion: a highly sensitive assay for prion detection, *Prion*, 2011, **5**(3), 150–153.
15 N. J. Haley, S. Carver, L. L. Hoon-Hanks, D. M. Henderson, K. A. Davenport, E. Bunting, *et al.*, Detection of chronic wasting disease in the lymph nodes of free-ranging cervids

by real-time quaking-induced conversion, *J. Clin. Microbiol.*, 2014, **52**(9), 3237–3243.

16 N. C. Ferreira, J. M. Charco, J. Plagenz, C. D. Orru, N. D. Denkers, M. A. Metrick 2nd, *et al.*, Detection of chronic wasting disease in mule and white-tailed deer by RT-QuIC analysis of outer ear, *Sci. Rep.*, 2021, **11**, 7702, DOI: 10.1038/s41598-021-87295-8.

17 D. Tewari, D. Steward, M. Fasnacht and J. Livengood, Detection by real-time quaking-induced conversion (RT-QuIC), ELISA, and IHC of chronic wasting disease prion in lymph nodes from Pennsylvania white-tailed deer with specific PRNP genotypes, *J. Vet. Diagn. Invest.*, 2021, **33**(5), 943–948, DOI: 10.1177/10406387211021411.

18 J. M. Wilham, C. D. Orru, R. A. Bessen, R. Atarashi, K. Sano, B. Race, *et al.*, Rapid end-point quantitation of prion seeding activity with sensitivity comparable to bioassays, *PLoS Pathog.*, 2010, **6**(12), e1001217.

19 A. H. Peden, L. I. McGuire, N. E. Appleford, G. Mallinson, J. M. Wilham, C. D. Orru, *et al.*, Sensitive and specific detection of sporadic Creutzfeldt-Jakob disease brain prion protein using real-time quaking-induced conversion, *J. Gen. Virol.*, 2012, **93**(2), 438–449.

20 C. Holz, J. R. Darish, K. Straka, N. Grosjean, S. Bolin, M. Kiupel, *et al.*, Evaluation of real-time quaking-induced conversion, ELISA, and immunohistochemistry for chronic wasting disease diagnosis, *Front. Vet. Sci.*, 2022, **8**, 824815, DOI: 10.3389/fvets.2021.824815.

21 N. C. Ferreira, J. M. Charco, J. Plagenz, D. O. Christina, N. D. Denkers, M. A. Metrick 2nd, *et al.*, Detection of chronic wasting disease in mule and white-tailed deer by RT-QuIC analysis of outer ear, *Sci. Rep.*, 2021, **11**, 7702, DOI: 10.1038/s41598-021-87295-8.

22 P. R. Christenson, M. Li, G. Rowden, P. Larsen and S. H. Oh, Nanoparticle-enhanced RT-QuIC (Nano-QuIC) diagnostic assay for misfolded proteins, *Nano Lett.*, 2023, **23**(8), 4074–4081.

23 G. R. Rowden, C. Picasso-Risso, M. Li, M. D. Schwabenlander, T. Wolf and P. Larsen, Standardization of data analysis for RT-QuIC-based detection of chronic wasting disease, *Pathogens*, 2023, **12**(2), 309, DOI: 10.3390/pathogens12020309.

24 M. V. P. Chowdary, K. K. Kumar, K. Thakur, A. Anand, J. Kurien, C. M. Krishna, *et al.*, Discrimination of normal and malignant mucosal tissues of the colon by Raman spectroscopy, *Photomed Laser Surg.*, 2007, **25**(4), 269–274.

25 A. Ditta, H. Nawaz, T. Mahmood, M. I. Majeed, M. Tahir, N. Rashid, *et al.*, Principal components analysis of Raman spectral data for screening of hepatitis C infection, *Spectrochim. Acta, Part A*, 2019, **221**, 117173.

26 I. K. Lednev, V. Shashilov and M. Xu, Ultraviolet Raman spectroscopy is uniquely suitable for studying amyloid diseases, *Curr. Sci.*, 2009, **97**(2), 180–185.

27 Y. Tan, B. Yan, L. Xue, Y. Li, X. Luo and P. Ji, Surface-enhanced Raman spectroscopy of blood serum based on gold nanoparticles for the diagnosis of oral squamous cell carcinoma, *Lipids Health Dis.*, 2017, **16**(1), 73.

28 C. Yu, E. Gestl, K. Eckert, D. Allara and J. Irudayaraj, Characterization of human breast epithelial cells by confocal Raman microspectroscopy, *Cancer Detect. Prev.*, 2006, **30**(6), 515–522.

29 Q. Wang, S. D. Grozdanic, M. M. Harper, K. Hamouche, N. Hamouche, H. Kecova, *et al.*, Detection and characterization of glaucoma-like canine retinal tissues using Raman spectroscopy, *J. Biomed. Opt.*, 2013, **18**(6), 067008.

30 Q. Wang, S. D. Grozdanic, M. M. Harper, N. Hamouche, H. Kecova, T. Lazic, *et al.*, Exploring Raman spectroscopy for the evaluation of glaucomatous retinal changes, *J. Biomed. Opt.*, 2011, **16**(10), 107006.

31 N. Mammadova, R. Kokemuller, C. Summers, Q. He, S. Ding, T. Baron, *et al.*, Accelerated accumulation of retinal α-synuclein (pSer129) and tau, neuroinflammation and autophagic dysregulation in a seeded mouse model of Parkinson's disease, *Neurobiol. Dis.*, 2019, **121**, 1–16.

32 H. Hu, J. Bai, G. Xia, W. Zhang and Y. Ma, Improved baseline correction method based on polynomial fitting for Raman spectroscopy, *Photonics Sens.*, 2018, **8**(4), 332–340.

33 E. B. Hanlon, I. Itzkan, R. R. Dasari, M. S. Feld, R. J. Ferrante, A. C. McKee, *et al.*, Near-infrared fluorescence spectroscopy detects Alzheimer's disease in vitro, *Photochem. Photobiol.*, 1999, **70**(2), 236–241.

34 B. E. Boser, I. M. Guyon, and V. N. Vapnik, A training algorithm for optimal margin classifiers, in *Proceedings of the Fifth Annual Workshop on Computational Learning Theory (COLT '92)*, New York (NY), ACM Press, 1992, pp. 144–152.

35 Azom.com, Using Raman spectroscopy to understand the conformational stability of protein therapeutics, 2014 [cited 2020 Oct 30], available from, https://www.azom.com/article.aspx?ArticleID=11142.

36 F. Pedregosa, G. Varoquaux, A. Gramfort, V. Michel, B. Thirion and O. Grisel, *et al.*, Scikit-learn: machine learning in Python, *arXiv*, 2012, preprint, arXiv [csLG] 1201.0490, DOI: 10.48550/arXiv.1201.0490, available from, http://arxiv.org/abs/1201.0490.

37 B. W. Barry, H. G. M. Edwards and A. C. Williams, Fourier transform Raman and infrared vibrational study of human skin: assignment of spectral bands, *J. Raman Spectrosc.*, 1992, **23**(11), 641–645.

38 G. P. Noble, D. W. Wang, D. J. Walsh, J. R. Barone, M. B. Miller, K. A. Nishina, *et al.*, A structural and functional comparison between infectious and non-infectious autocatalytic recombinant PrP conformers, *PLoS Pathog.*, 2015, **11**(6), e1005017.

39 C. Pan, B. Zhu and C. Yu, A dual immunological Raman-enabled crosschecking test (DIRECT) for detection of bacteria in low-moisture food, *Biosensors*, 2020, **10**(12), 200.

40 M. Kahraman, A. I. Zamaleeva, R. F. Fakhrullin and M. Culha, Layer-by-layer coating of bacteria with noble metal nanoparticles for surface-enhanced Raman scattering, *Anal. Bioanal. Chem.*, 2009, **395**(8), 2559–2567.